The effect of scan speed and hatch distance on prior-beta grain size in laser powder bed fused Ti-6Al-4V

D.F. Louw and P.G.H Pistorius

Abstract Ti6Al4V produced by laser powder bed fusion can achieve mechanical properties similar to its wrought counterpart if an appropriate post process heat treatment is applied. The response of the material to post process heat treatment depends on the prior-beta grain size in the as-built condition. The current article illustrates that a reduction in hatch distance can cause coarsening of prior-beta grain due to retained heat that reduces the cooling rate. On the other hand, an increase in scan speed refines prior-beta grains. Unfortunately, an increase in scan speed has to be accompanied by a reduction in hatch distance to prevent an increase in porosity and the potential grain refinement is then cancelled out. The use of a faster scan speed in combination with a smaller hatch distance significantly improves roughness of the top surface. EBSD in combination with re-construction of prior-beta grains is an effective technique to quantify prior-beta grain size. Furthermore, the use of Rosenthal's equations allows quick calculation of cooling rate that can be used to predict the dependence of prior-beta grain size on process parameters.

Keywords Laser Powder Bed Fusion · Titanium Metallurgy · Selective Laser Melting · Additive Manufacturing

D.F Louw
Council for Scientific and Industrial Research(CSIR), Meiring Naude Road, Pretoria
Tel.: +2712-841-4136
E-mail: dlouw@csir.co.za

P.G.H Pistorius
University of Pretoria, Lynnwood Road, Pretoria
Tel.:+2712-420-3186
E-mail: pieter.pistorius@up.ac.za

1 Introduction

Laser powder bed fusion (LPBF) is an additive manufacturing technology capable of producing functional metal components [1]. A component is formed on top of a solid base plate (with thickness typically around 30 mm) that is usually made of the same material as the part. The process starts by spreading a thin layer (around 50 μm) of fine spherical metal powder on top of the base plate after which, a laser beam selectively melts the powder to form a cross section of the component being produced. The building platform is then lowered by a distance equal to the layer thickness, a new layer of powder is deposited by a powder-layering mechanism and the process is repeated. By repeatedly melting thin layers on top of one another, a component firmly attached to the base plate is formed. Compared to other additive manufacturing techniques, LPBF can achieve fine resolution and offers more dimensional freedom since the powder provides inherent support [1,2]. It is of particular interest to investigate LPBF of Ti6Al4V due to its good strength to weight ratio, good weldability and the fact that it is the most widely used titanium alloy [3]. On the other hand, the ability of LPBF to produce components that are designed to be light weight makes it an ideal combination of process and material.

From a metallurgical point of view, LPBF is characterised by fast cooling rates and large thermal gradients [4]. In the as-built condition, Ti6Al4V has high yield strength (around 1100 MPa), but low ductility (between 3 and 10 percent elongation to break) with a microstructure that consists of martensite inside columnar prior-beta grains [5–11]. Numerous studies have looked at how the poor mechanical performance in the as-built condition can be improved by appropriate post processing techniques. An annealing heat treatment at 850 or 900 ^{o}C was shown to change the marten-

site into a lamellar mixture of alpha and beta where the length of the largest lamella is limited by the size of the prior-beta grains [6, 12]. Such a microstructure has improved ductility but exhibits lower yield strength. When heat treatment is performed at temperatures closer to the beta transus (950 ^{o}C) it was observed that fragmentation of alpha lamella occur at twinning dislocations and prior-beta grain boundaries, resulting in improved ductility[7]. The response of Ti6Al4V to post process heat treatment therefore depends on the prior-beta grain size and the number of beta grain boundaries in the as-built condition. Previous research has focussed on characterising the microstructure of Ti6Al4V processed by LPBF and also studied the effects of scan speed, hatch spacing, scan strategy and inter-layer time on the microstructure [5,9]. It was found that the time between layers, the energy density and the focal offset distance can determine if a martensitic or fine lamellar microstructure is produced [9,13]. Furthermore, it was found that when a bi-directional scan strategy (that is kept in the same direction between layers) is used, the widths of columnar prior beta grains depends on scan speed in the direction of scanning [5]. In such a case it was also observed that the width of prior-beta grains perpendicular to the scan direction depends on the hatch distance [5]. The current article aims to refine prior-beta grain size by increasing scan speed and decreasing hatch distance.

Ti6Al4V solidifies at around 1670 ^{o}C as beta crystals. As these crystals cool to below the beta-transus temperature of 995 ^{o}C [3] the microstructure changes to a lamellar mixture of alpha and beta phase. At high cooling rates (above 410 ^{o}C/s) a fully martensitic microstructure forms [14]. In order to investigate prior-beta grains the conditions that govern solidification need to be considered. It is known that when molten metal solidifies, faster cooling rates create more sites that are energetically favourable for nucleation of crystals. Every crystal that nucleates grows until it is impinged upon by a neighbouring crystal. Therefore faster cooling rates result in smaller grains [15] in the final material. The effect of cooling rate on prior-beta grain size in Ti6Al4V has been experimentally shown to follow a power law relationship [16] by splat quenching of individual metal droplets. It should be noted that in these experiments individual particles were cooled separately and no epitaxial growth could take place. In LPBF, epitaxial growth of crystals is almost un-avoidable [4]. In the process of LPBF where a moving heat source locally melts material the cooling rate depends on the heat flux(which is the amount of absorbed laser power in the case of LPBF), scan speed and temperature of the underlying material (similar to welding). The effect of scan speed and laser power can be combined by calculating the heat input which is the amount of absorbed energy per unit length. Any two single tracks that is produced with the same heat input should experience the same cooling rate if the temperature of the base material is the same in both cases. The current study investigates the effect of process parameters on the prior beta grain size in Ti6Al4V produced by LPBF.

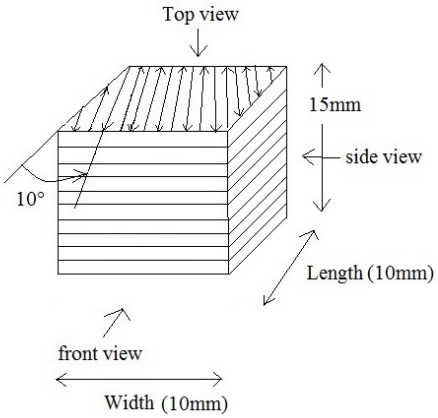

Fig. 1 Diagram illustrating the scan direction used and views considered

2 Experimental methods

Spherical Ti6Al4V powder with an average powder particle size of 40 μm and maximum of 60 μm was used. The powder was procured from TLS Technik GmbH and Co. The samples were produced by the high power, high speed Aeroswift LPBF machine at South Africa's Council for Scientific and Industrial Research's National Laser Centre. A standard parameter set was used as starting point. Due to confidentiality of the process parameters, scan speed is reported as multiples of the standard scan speed and the hatch distance is reported as percentage overlap of the laser spot. A full factorial experimental matrix with 5 scan speeds and 3 hatch distances was tested. From the full factorial experimental matrix, samples with acceptably low levels of porosity were identified and examined further by considering prior-beta grain size. The normalised parameters used are given in Table 1. The heat input (HI) was calculated with the following equation:

$$HI = P/v \tag{1}$$

With P = absorbed laser power (it was assumed that 90 percent of the laser power is absorbed), v = scan speed. All samples were produced with the same laser power, layer thickness and with a bi-directional scan strategy that was not rotated between layers. The base plate was preheated to 200 ^{o}C. The samples were produced as rectangular blocks with dimensions 10 mm x 10 mm x 15 mm. The scan direction relative to the sides of the blocks is shown in Fig. 1. No contour scan along the edge of a layer was performed. The building direction is from bottom to top in all side view

Table 1 Parameters used and the corresponding dimensions and roughness of each sample. Labels given to samples in this table will be used consistently throughout the text.

Sample ID	Scan factor	Percentage overlap	Length(mm)	Width(mm)	Height(mm)	Roughness Ra(μm)	Heat input(J/mm)
a	1	50	10.6	10.5	15.1	10	0.45
b	1.25	50	10.6	10.5	15.1	11	0.36
c	1.5	50	10.7	10.4	15	12	0.3
d	1.75	50	10.7	10.4	14.9	16	0.26
e	2	50	10.7	10.3	15	n.a.*	0.23
f	1	65	10.7	10.5	14.9	6	0.45
g	1.25	65	10.7	10.4	14.9	6	0.36
h	1.5	65	10.7	10.5	14.9	7	0.3
i	1.75	65	10.7	10.4	14.9	8	0.26
j	2	65	10.7	10.4	14.9	9	0.23
k	1	80	10.7	10.7	14.9	5	0.45
l	1.25	80	10.8	10.7	14.9	5	0.36
m	1.5	80	10.8	10.6	15	5	0.3
n	1.75	80	10.9	10.5	14.9	5	0.26
o	2	80	10.9	10.6	14.9	6	0.23

*Surface roughness exceeded the limit of the measuring device

micrographs. For side view micrographs samples were sectioned so that the face to be viewed is 5mm from the edge. The scan direction is 10 degrees from the horizontal in the top view micrographs. For top view micrographs samples were sectioned so that the face to be viewed is 7.5mm from the top. Samples were ground manually in sequence with 80, 310, 1200 and 4000 grit SiC grinding paper. Each step grinding was done until all scratches were in one direction after which it was rotated by 90 degrees for the next grinding step and again ground until the new scratches were in one direction. Thereafter polishing was done with 0.04 μm colloidal silica suspension until all scratches were removed. Etching was done for 10 seconds with Kroll's reagent. Sample preparation for EBSD consisted of grinding down to a grit size of 1000 followed by electro-polishing. EBSD was performed with a Zeiss Cross-Beam 540 microscope equipped with an Oxford Aztec HKL EBSD detector. An accelerating voltage of 20 kV was used together with a beam current of 10 nA. Mapping was done with a step size of 1 μm. EBSD data was processed with Mtex toolbox in Matlab to reconstruct prio-beta grains.

The roughness of the top surface of each sample was measured with a Marsurf PS1 roughness tester. The travel length of the probe set to 5.6mm and the number of sampling points set to 5. Each surface was measured 25 times and the average reported. All roughness measurements were done with the probe travelling along the length of samples. The height of each sample was measured with a height gauge while it was still attached to the base plate. Samples were cut from the base plate by wire-cutting and thereafter put in an ultrasonic bath for 15 minutes to remove loose powder after which density measurements were performed with a OHAUS weight balance equipped with a density measurement kit. Acetone was used as immersion liquid to prevent bubbles from being trapped on the surface. In order to compensate for temperature variations that may occur in the liquid, a wrought Ti-grade 5 sample of the same dimensions was measured immediately before each measurement and the density of the wrought sample was taken as 100 percent dense to calculate percentage porosity. The density of each sample was measured 3 times with the average reported. The width and length of each sample was measured with a vernier calliper after removal from the base plate. Vickers microhardness was measured with a Zwick/Roell ZHVμ hardness tester. The instrument was set to automatically indent every 1mm along the build direction. A load of 300g with 10s dwell time was used.

3 Results

3.1 Porosity, surface roughness and dimensional accuracy

The measured surface roughness and dimensions of each sample are summarised in Table 1. It is seen that surface roughness is higher for samples produced at low scan speed than at high scan speed. It is also seen that surface roughness is higher for samples produced with low percentage overlap than with high percentage overlap. Sample length slightly increases with scan speed while width slightly decreases. By comparing samples (a), (f) and (k) it is seen that length and width increase with percentage overlap. Variations in height between different samples do not show a clear dependence on process parameters. The slight variations between sample heights may be due to non-perfect levelling of the base plate before processing. Shown in Fig. 2 is percentage porosity as a function of scan factor. Samples with less than 0.5 percentage porosity are reported. Note that porosity increases with scan speed but decreases with percentage overlap. Further-

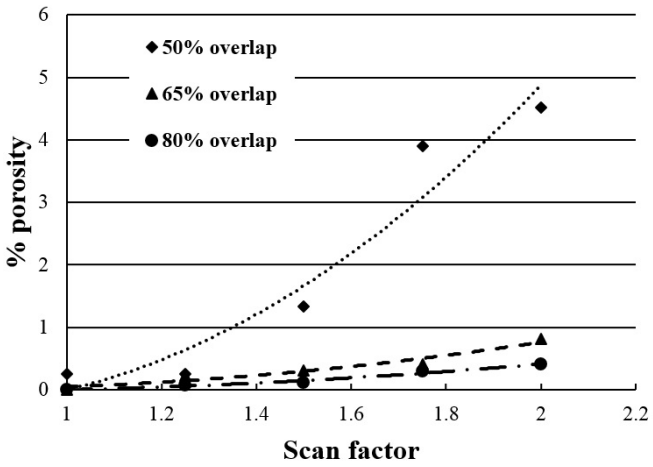

Fig. 2 Percentage porosity as function of scan factor and percentage overlap with second order polynomial regression curves shown

more, note that when a larger percentage overlap is used, samples with low porosity can be produced at faster scan speeds. The observed quadratic relationship between percentage porosity and scan speed is in agreement with observations from other researchers [17].

3.2 Side view microstructure and micro hardness

Microstructures of the various samples as shown in Fig. 3 confirm an increase in percentage porosity with scan speed. It is also confirmed that at larger percentage overlap low percentage porosity can be achieved at higher scan speeds. It is seen that at 80 percent overlap a 1.5x increase in scan speed does not cause porosity to occur. Note that even though samples (h), (i) and (j) have less than 0.5 percent porosity and may seem to be promising parameters the pores have a flat elongated shape that will act as a stress raiser and have a detrimental effect on mechanical properties. A martensitic phase inside columnar grains is observed in all samples which is typical of Ti6Al4V produced with additive manufacturing [5]. The columnar prior-beta grains are more or less vertical as one would expect for the bi-directional scanning strategy that was used [5]. The effect of percentage overlap on the microstructure is best illustrated by comparing samples (a), (f) and (k)(i.e. the top row in Fig. 3). Coarsening of the prior beta grains is observed at higher percentages overlap. Furthermore, light lines that run horizontally are observed at 80 percent overlap. These lines are roughly spaced 50 micrometers apart which corresponds to the layer thickness that was used and are the heat affected zones of a layer caused by the subsequent layer. The effect of scan speed on the size of prior beta grains is best illustrated by comparing samples (k), (l), (m), (n) and (o) i.e. the right most column of Fig. 3. Firstly, note that an increase in scan speed results in finer and more irregular shaped prior beta grains. Secondly, note that the horizontal lines from the layer wise heating become fainter with an increase in scan speed. Note that a 2x increase in scan speed produces flat elongated pores that indicates lack of fusion between the layers.

Hardness measurements are reported in Fig. 4 and 5. Firstly, note that for all the samples a hardness of roughly 380 Hv was measured. This is a typical hardness value for Ti6Al4V produced by LPBF [5]. Secondly, note that Fig. 4 illustrates no clear relationship between percentage overlap and hardness. The light horizontal lines seen in Fig. 3 (k) that is attributed to the layer wise heating effects may only become apparent if hardness indents are placed closer together and made with much lower loads. The typical size of the indents used in this study was around 40μm. There is also no clear variation in hardness along the building direction. Despite percentage overlap not affecting hardness, there seem to be a relationship between scan speed and hardness. Note that in Fig. 5 the samples produced at faster scan speeds consistently have higher hardness.

3.3 Top view microstructure

Shown in Fig. 6 are the microstructures as seen from the top of samples a, f and k (see Table 1 for sample labels). The micrographs show the top view, with the scanning direction tilted 10 degrees with the horizontal axis. Firstly note that similar to the side view microstructures a larger percentage overlap results in a coarser microstructure. Peculiarly, the prior-beta grains does not appear to be slanted towards the scanning direction and no herringbone pattern is seen as one would expect for a bi-directional scan strategy that is kept constant throughout the layers. It is also not possible to identify the track width as reported by other researchers [5,6].

3.4 EBSD and prior-beta grain reconstruction

In order to achieve more accurate quantitative results about prior-beta grain size, EBSD together with re-construction of prior-beta grains was performed. It was decided to select only the standard sample, sample a in Table 1, for analysis by EBSD. Results are shown in Fig. 7. Fig. 7 (a) shows a map of the raw orientation data of alpha phase with white pixels representing un-indexed data points. Fig. 7 (b) shows the reconstructed beta grains overlaid on the alpha grains. Prior-beta grain boundaries with misorientation angles greater than 10^o are highlighted in black in Fig. 7 (b). The misorientation density plot of the alpha phase is shown in 7 (c), expected peaks at misorientations of 10.5, 60, 60.8, 63.3 and 90 relating to alpha variants inherited from the same parent beta grain is seen [18]. From the reconstructed map it is observed that prior-beta grains vary between 25 and 100 μm in

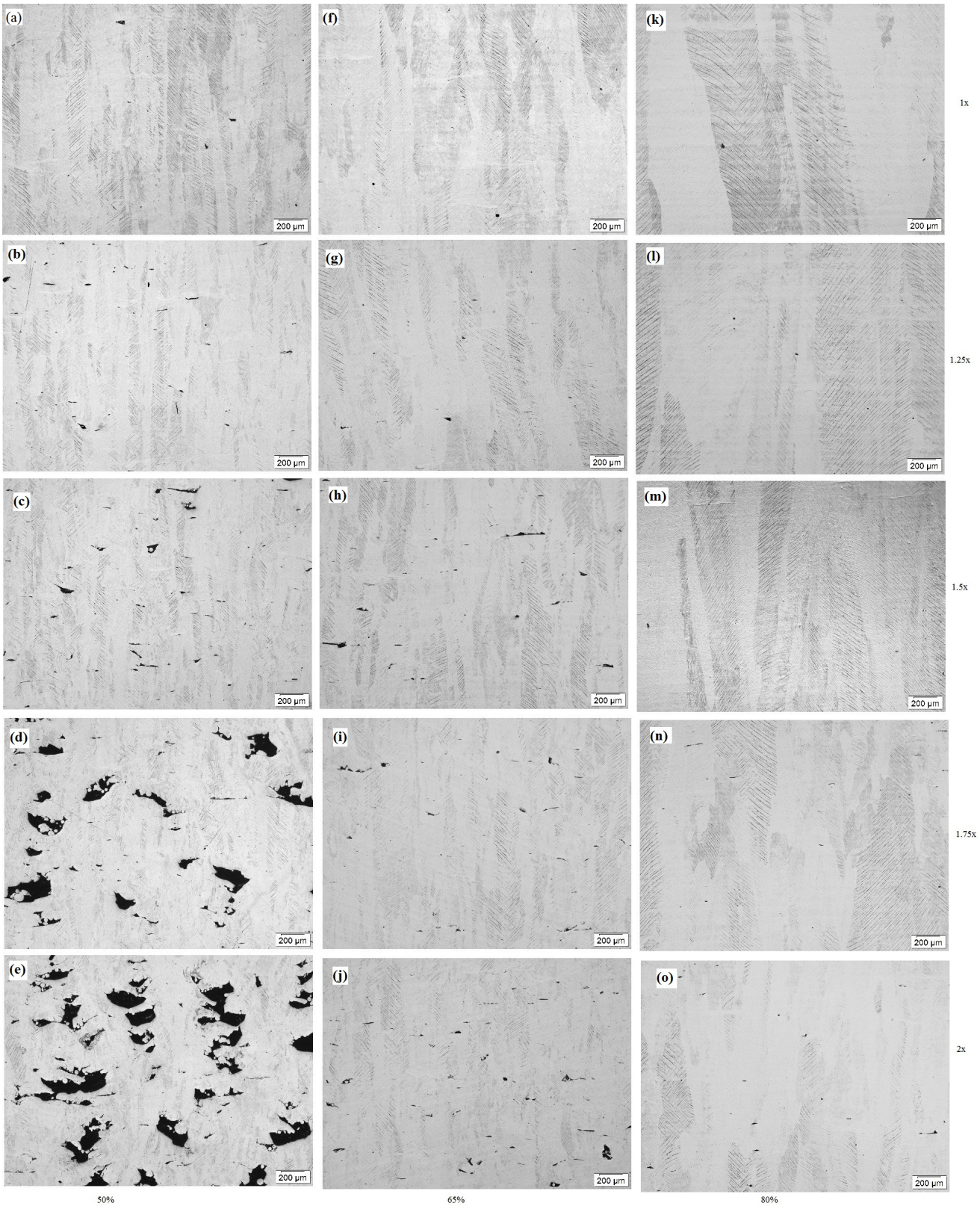

Fig. 3 Side view microstructures of the various samples, samples are labelled according to parameters specified in table 1, samples are separated according to percentage overlap in columns and scan factor in rows, see labels on side and bottom

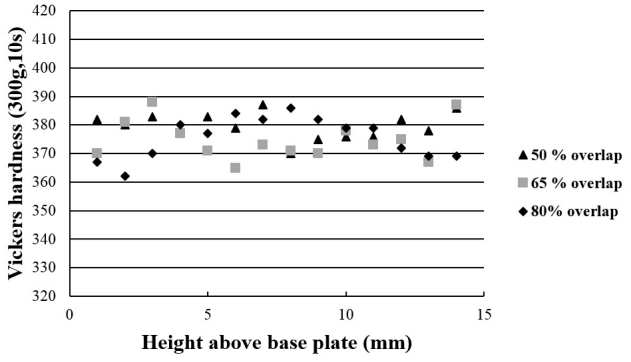

Fig. 4 Hardness along building direction for samples with different percentages overlap, all samples reported in this graph were produced at the standard 1x scan speed

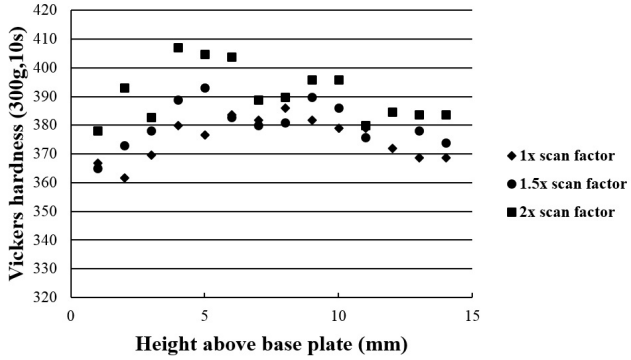

Fig. 5 Hardness along building direction for samples with different scan speeds, all samples reported in this graph were produced at 80 percent overlap

size which confirms observations from optical microscopy. It was possible to index only 59 percent of the pixels due to fact that each pixel was 1 μm in size while many of the needles in the martensitic structure was smaller than 1μm as seen in the band contrast image in Fig. 8. Out of the indexed pixels 98.5 percent was identified as alpha phase and 1.5 percent as beta phase.

4 Discussion

4.1 Dimensional properties, roughness, porosity, microstructure and hardness

The effects of scan speed and percentage overlap on surface roughness and porosity can be imagined by considering the multiple adjacent single tracks that make up each layer [19]. If scan speed is increased the track width decreases. When the track width decreases the gap between top beads of adjacent track becomes larger which increases surface roughness and porosity, by the same mechanism a larger overlap decreases surface roughness and porosity [20]. Furthermore, if scan speed is increased enough, each single track forms detached balls of solidified metal which will increase both surface roughness and percentage porosity. The occurrence of flat pores at high scan speeds despite large overlap is an indication that at such speeds insufficient heat is supplied for penetration through the powder layer. Such flat pores does not significantly increase the percentage porosity but acts as a stress raisers under load which may cause premature failure. [21] The observed decrease in sample width with increasing scan speed is also a result of the reduction in track width with increasing scan speed. The increase in sample length with increasing scan speed may be due to incorrect timing of the laser for the start and end points of every track at such high scan speeds. The use of a contour scan may eliminate the latter effect. The increase of sample length with increasing percentages overlap may be due to more retained heat at the ends of tracks in the case when larger overlap is used that in turn increases the melt pool size. Once more it should be noted that such effects will become irrelevant if a contour scan is used.

The observed martensitic microstructure forms as a result of fast cooling rates. Cooling rates typically involved in LPBF are orders of magnitude more than the 410 ^{o}C/s required for martensite formation in Ti6Al4V. Some estimates of cooling rates involved in LPBF of metals are around 10^{7} ^{o}C/s [22]. On the other hand, the observed columnar prior beta grains grow epitaxially from one layer to the next which is why one grain can be several times longer than the layer thickness. In order to understand the effects of parameters on prior beta grain width it is recalled that nucleation and growth for the case where a moving heat source melts the material depends on the heat input and temperature of the underlying material. The effect of a reduction in grain size with increasing scan speed is a direct result of the lower heat input that results in faster cooling rates that the melt pool experiences. The same effect has been observed by other researchers [5]. The occurrence of more irregular grains at high scan speeds may be as a result of balling of single tracks. To understand the effect of overlap on prior beta grain size, the temperature surrounding the melt pool at the position in the sample where microstructures were investigated needs to be considered. Every piece of the material being produced experience a local thermal cycle and a global thermal cycle. The local thermal cycle referred to is caused by the heat from adjacent tracks. The global thermal cycle refers to changes in temperature of the base plate and underlying sample as the build progresses. If significant changes in the global temperature of the sample occurred, this should be seen as a variation in microstructure between the top and bottom of the sample while local changes should be seen as effects that are the same distance apart as the layer thickness. The observed coarsening that is seen at larger overlap is a result of more tracks being scanned in the same area that increases

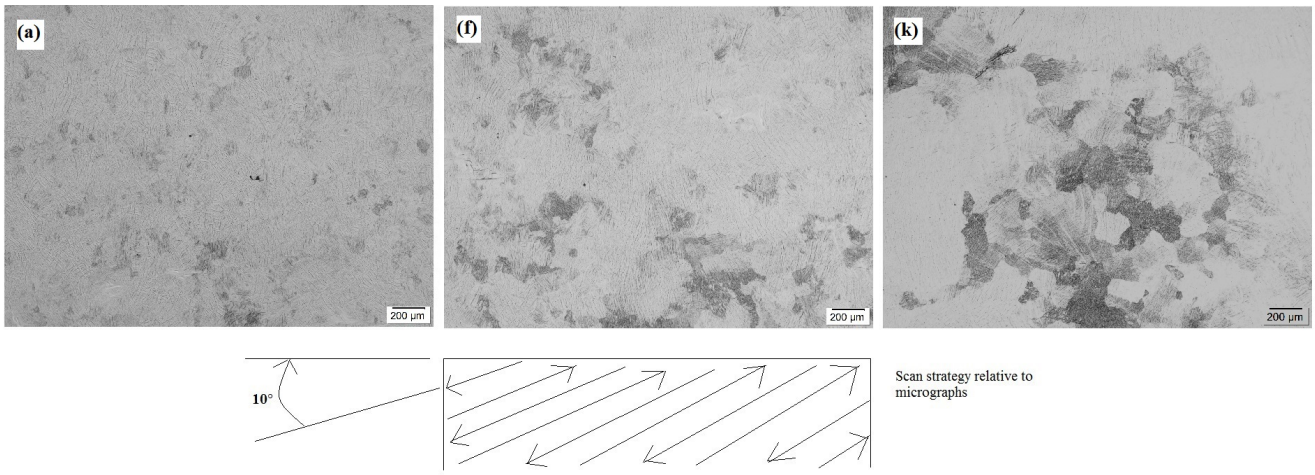

Fig. 6 Microstructures of top view of samples with 50 percent(a), 65 percent(f), and 80 percent(k) overlap, Labels correspond to table 1, the scanning direction relative to the microstructures is illustrated in the schematic

the local temperature so that the cooling rate during solidification and the grain size is affected. This explanation is supported by the horizontal lines that become more pronounced at larger percentage overlap and by theoretical calculations in the next section. The absence of a clear rise or fall in the micro-hardness along the building direction is an indication that the change in temperature of the base plate and underlying sample as the build progress is not significant enough to have an effect on microstructure. The effect of scan speed on hardness as illustrated in Fig. 4 may be an indication that at lower scan speeds enough heat is supplied to have a tempering effect on underlying material, but if this was the case one should see the same effect by an increase in overlap. The increase in hardness with increasing scan speed is also in contrast to observations by other researchers [5].

It is interesting to note the one-to-one relationship between hatch distance and grain width in the top view that was observed by other researchers [5] is not seen in the top view microstructures shown in Fig. 6. Potential explanations for the latter effect may be that at large percentages overlap, epitaxial growth of prior-beta grains between adjacent single tracks in one layer occurs.

Observed peaks in the misorientation density plot corresponds to alpha variants that are inherited from the same parent beta grain according to the Burgers orientation relationship. Theoretically misorientation angles between variants that form during transformation of bcc to hcp obeying the Burgers oriantation relation are 10.5 ^{o}, 60 ^{o}, 60.8 ^{o}, 63.2 ^{o} and 90 ^{o} [18]. It is this relationship that was used to reconstruct the prior-beta grains shown in Fig. 7 (b). If it occurred that the sample experienced significant plastic strain due to the thermal cycles of the process, the orientation relationship would not have been clear.

4.2 Theoretical calculation of cooling rate and prior-beta grain size

The observed effects can be compared to theoretical calculations of cooling rate as function of different process parameters. Temperature (T) as a function of time (t) at a distance r from the centre of the meltpool can be approximated with the Rosenthal equation for a moving heat source in an infinitely thick plate as stated below:

$$T = \frac{P/v}{2\pi kt} \exp -\frac{r^2}{4at} + T_0 \tag{2}$$

With P = absorbed laser power, v = scan speed, k = thermal conductivity, T_0 = temperature of the surrounding material, and a = thermal diffusivity. If the point in the middle of the melt pool is considered, $r = 0$ the equation simplifies to:

$$T = \frac{P/v}{2\pi kt} + T_0 \tag{3}$$

By solving equation 3 for t, the time that it takes for the material to cool to the freezing temperature T_F can be expressed as:

$$t = \frac{P/v}{2\pi k(T_F - T_0)} \tag{4}$$

The infinitely high temperature in the centre of the melt pool as predicted by the Rosenthal equation is avoided by looking only at the cooling rate at the freezing temperature which will always be a distance away from the middle of the melt pool. By differentiating equation 3 with respect to time the cooling rate $\dot{T}$ can be expressed as:

$$\dot{T} = \frac{dT}{dt} = -\frac{P/v}{2\pi kt^2} \tag{5}$$

Substituting equation 4 into 5 and simplifying, shows that cooling rate at freezing is:

$$\dot{T} = (v/P)2\pi k(T_F - T_0)^2 \tag{6}$$

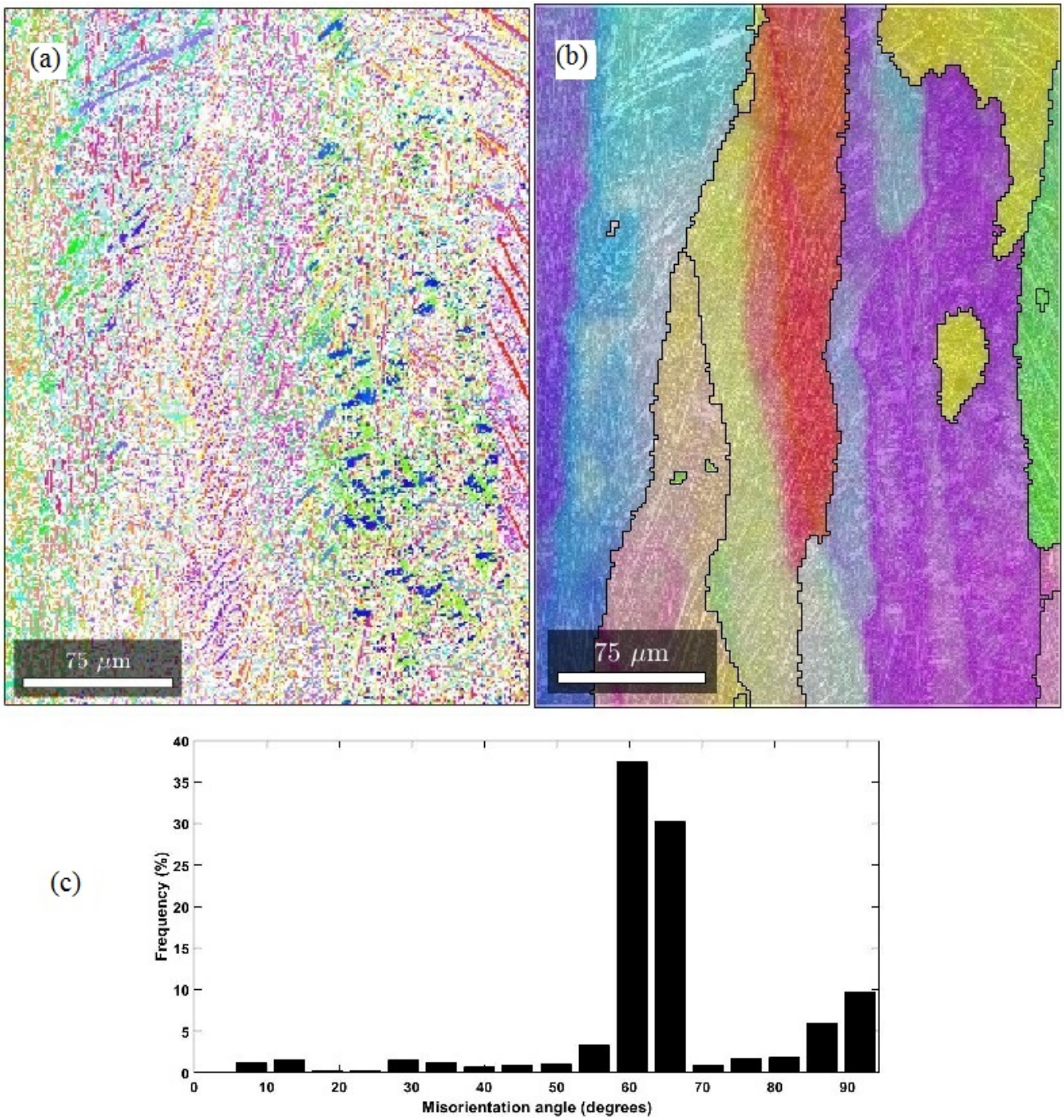

Fig. 7 (a) Orientation Map of alpha needles (b) Overlay of reconstructed prior-beta grains on top of alpha grains map (c) Misorientation density plot of alpha grains

In order to determine T_{0_n} the temperature of the base material surrounding the nth track in a layer the following equation derived from equation 2 was used:

$$T_{0_n} = \sum_{i=1}^{i=n} \frac{P/v}{2\pi k i t_{track}} \exp\left(-\frac{(ih)^2}{4ait_{track}}\right) + T_0 \tag{7}$$

Where h is the hatch distance and t_{track} the time that passed between the scanning of adjacent tracks. Furthermore, prior-beta grain size can be calculated from cooling rate with the following equations [16]: The lower limit of the expected prior-beta grain size in (μm):

$$L = 3.1 * 10^6 * \dot{T}^{-1.05} \tag{8}$$

The upper limit of the expected beta grain in (μm):

$$L = 3.1 * 10^6 * \dot{T}^{-0.81} \tag{9}$$

Table 2 Parameters used and the corresponding predicted temperature of material surrounding track in middle of sample and calculated prior-beta grain width ranges

Sample ID	Scan factor	Heat input (J/mm)	Percentage overlap	$T_{0_{middle}}(^{o}C)$*	Cooling rate $^{o}C/s$	Prior-beta grain width (μm)
a	1	0.45	50	521	126 000	14 - 230
f	1	0.45	65	627	104 000	16 - 268
k	1	0.45	80	779	76 000	23 - 345
l	1.25	0.36	80	760	99 000	18 - 279
m	1.5	0.3	80	742	123 000	14 - 233
n	1.75	0.26	80	730	148 000	12 - 202
o	2	0.23	80	709	176 000	10 - 175

*Temperature of material surrounding track in middle of sample

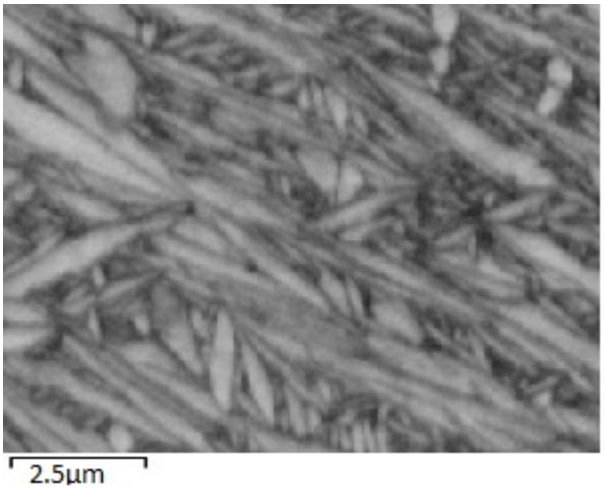

Fig. 8 Band contrast image of fine alpha needles

Where L is the prior beta grain size which is the width in the case of LPBF where epitaxial growth occurs.

With the use of equation 5 cooling rate in the middle of the sample, for samples produced with different hatch distances and different scan speeds was calculated which in turn allowed prior beta grain size to be calculated with the help of equations 7 and 8. Freezing temperature was taken as 1953K, the thermal conductivity at 6.7 W/(mK) and the thermal diffusivity as $2.87x10^{-6}m^2/s$ and it was assumed that 90 percent of the applied laser power is absorbed. The results are reported in Table 2. It is seen that the coarsening trends observed in the microstructure shown in Fig. 3 is also predicted theoretically in Table 2. Exact values of grain size is difficult to compare with theoretical predictions due to the difficulty in clearly identifying prior beta grains boundaries. The effect of hatch distance appears to be under-estimated by the calculations. Note that even though sample o was produced with half of the linear heat input that was used to produce sample a the cooling rate is not significantly more. The reason for this is that sample o was produced with a smaller hatch distance and less time between adjacent tracks which raised the temperature of the surrounding material. Despite fairly good correlation between theory and experiment care must be exercised when accepting cooling rates predicted by Rosenthal equations because it ignores effects such as temperature dependant material properties, fluid flow in the melt pool, latent heat of phase changes and heat loss by convection, radiation or evaporation. However, findings by other researchers [23] suggest Rosenthal equations to be good approximations and gives the reader confidence that the explanations given for the observed trends are correct.

5 Conclusions

Based on the results obtained a few conclusions can be drawn. For a given combination of laser power, spot size, layer thickness, scan speed and hatch distance it is possible to increase scan speed and at the same time reduce hatch distance to achieve a smoother top surface without a change in porosity. However, this approach at process improvement does not significantly refine the prior-beta grains. Prior beta grain size increases if hatch distance is decreased duo to heat build-up by adjacent tracks. Prior beta grain size decrease with scan speed due to faster cooling rates. At large percentages overlap epitaxial growth of grains occur between adjacent tracks in the same layer. EBSD in combination with prior-beta grain reconstruction is a good method for quantifying the as-built microstructure, Rosenthal equations for a moving heat source provides quick calculations to approximate cooling rate and prior-beta grain size.

Acknowledgements The authors would like to thank funding provided by South Africa's Department of Science and Technology through the Collaborative Program in Additive Manufacturing. Furthermore, laboratory and equipment support from CSIR, University of Pretoria and Aeroswift ADC is acknowledged. Prior-beta grain reconstruction by Gerrit Ter Haar is acknowledged.

References

1. Wohlers T, Campbell I, Diegel O, Kowen J(2018) Wohlers Report 2018. Wohlers Associates Inc., United States of America
2. Levy GN (2010) The role and future of the Laser Technology in the Additive Manufacturing environment. Physics Procedia 5:65-80

3. Lutjering G, Williams JC (2003) Titanium. Springer-Verlag Berlin Heidelberg, Germany
4. Rombouts M (2006) Selective Laser Sintering/Melting of iron-based powders. Dissertation, Katholieke Universiteit Leuven
5. Thijs L, Verhaeghe F, Craeghs T, Van Humbeeck J, Kruth JP (2010) A study of the microstructural evolution during selective laser melting of Ti-6Al-4V. Acta Matrialia 58:3303-3312
6. Vrancken B, Thijs L, Kruth JP, Van Humbeeck J (2012) Heat treatment of Ti6Al4V produced by Selective Laser Melting: Microstructure and mechanical properties. Journal of Alloys and Compounds 541:177-185
7. Ter Haar GM, Becker TH(2018) Selective Laser Melting Produced Ti-6Al-4V: Post-Process Heat Treatments to Achieve Superior Tensile Properties. Materials 11:146
8. Leuders S, Thöne M, Riemer A, Niendorf T, Tröster T, Richard HA, Maier HJ(2013) On the mechanical behaviour of titanium alloy TiAl6V4 manufactured by selective laser melting: Fatigue resistance and crack growth performance. International Journal of Fatigue 48:300-307
9. Xu W, Lui EW, Pateras A, Qian M, Brandt M(2017) In situ tailoring microstructure in additively manufactured Ti-6Al-4V for superior mechanical performance. Acta Materialia 125:390-400
10. Qiu C, Adkins NJE, Attallah MM(2013) Microstructure and tensile properties of selectively laser-melted and of HIPed laser melted Ti-6Al-4V. Materials Science and Engineering A 578:230-239
11. Rafi HK, Karthik NV, Gong H, Starr TL, Stucker BE (2013) Microstructure and Mechanical Properties of Ti6Al4V Parts Fabricated by Selective Laser Melting and Electron Beam Melting, Journal of Materials Engineering and Performance. https://doi.org/10.1007/s11665-013-0658-0
12. Kasperovich G, Hausmann J (2015) Improvement of fatigue resistance and ductility of Ti6Al4V processed by selective laser melting. Journal of Materials Processing Technology 220:202-214
13. Xu W, Brandt M, Sun S, Elambasseril J, Lui Q, Latham K, Xia K, Qian M(2015) Additive manufacturing of strong and ductile Ti-6Al-4V by selective laser melting via in situ martensite decomposition. Acta Materialia 85:74-84
14. Ahmed T, Rack HJ(1998) Phase transformations during cooling in Alpha + Beta titanium alloys. Materials Science and Engineering A243:2016-211
15. Chadwick GA (1972) Metallography of phase transformations. Butterworth and Co South Africa Pty Ltd, South Africa
16. Broderick TF, Jackson AG, Jones H, Froes FH (1985) The Effect of Cooling Conditions on the Microstructure of Rapidly Solidified Ti-6Al-4V. Metallurgical Transactions A 16A:1951-1959
17. Kamath C, El-dasher B, Gallegos GF, King WE Sisto A, (2014) Density of additively-manufactured, 316L SS parts using laser powder-bed fusion at powers up to 400W. International Journal of Advanced Manufacturing Technology. https://doi.org/10.1007/s00170-014-5954-9
18. Karthikeyan T, Saroja S, Vijayalakshmi M (2006) Evaluation of misorientation angle-axis set between variants during transformation of bcc to hcp phase obeying Burgers orientation relation. Scripta Materialia 55:771-774
19. Yadroitsev I, Smurov I (2010) Selective laser melting technology: from single laser melted track stability to 3D parts of complex shape. Physics Procedia 5:551 -560
20. Tang M, Pistorius PC, Beuth JL (2017) Prediction of lack-of-fusion porosity for powder bed fusion. Additive Manufacturing 14:39-48
21. Tang M, Pistorius PC (2017) Oxides, porosity and fatigue performance of AlSi10Mg parts produced by selective laser melting. International Journal of Fatigue 94:192-201
22. Thijs L, Sistiaga MLM, Wauthle R, Xie Q, Kruth JP, Van Humbeeck J (2013) Strong morphological and crystallographic texture and resulting yield strength anisotropy in selective laser melted tantalum. Acta Materialia 61:4657-4668
23. Promoppatum P, Yao SC, Pistorius PC, Rollett AD (2017) A Comprehensive Comparison of the Analytical and Numerical Prediction of the Thermal History and Solidification Microstructure of Inconel 718 Products Made by Laser Powder-Bed Fusion. Engineering 3:685-694